Multicellular density fluctuations in epithelial monolayers

Steven M. Zehnder,[1] Marina K. Wiatt,[2] Juan M. Uruena,[1] Alison C. Dunn,[3] W. Gregory Sawyer,[1] and Thomas E. Angelini[1,4,5]

[1]*Department of Mechanical and Aerospace Engineering, University of Florida, Gainesville, Florida 32611, USA*

[2]*Department of Chemical Engineering, University of Florida, Gainesville, Florida 32611, USA*

[3]*Department of Mechanical Science and Engineering, University of Illinois, Champaign-Urbana, Illinois 61801, USA*

[4]*J. Crayton Pruitt Family Department of Biomedical Engineering, University of Florida, Gainesville, Florida 32611, USA*

[5]*Institute for Cell Engineering and Regenerative Medicine, University of Florida, Gainesville, Florida 32611, USA*

(Received 16 January 2015; revised manuscript received 5 August 2015; published 30 September 2015)

Changes in cell size often accompany multicellular motion in tissue, and cell number density is known to strongly influence collective migration in monolayers. Density fluctuations in other forms of active matter have been explored extensively, but not the potential role of density fluctuations in collective cell migration. Here we investigate collective motion in cell monolayers, focusing on the divergent component of the migration velocity field to probe density fluctuations. We find spatial patterns of diverging and converging cell groups throughout the monolayers, which oscillate in time with a period of approximately 3–4 h. Simultaneous fluorescence measurements of a cytosol dye within the cells show that fluid passes between groups of cells, facilitating these oscillations in cell density. Our findings reveal that cell-cell interactions in monolayers may be mediated by intercellular fluid flow.

DOI: 10.1103/PhysRevE.92.032729 PACS number(s): 87.17.Jj, 87.18.Gh, 87.18.Hf

I. INTRODUCTION

Cell size is strongly coupled to motion in developing tissue and in cancer [1]. During morphogenesis in embryonic models, regional changes in cell volume drive large-scale motion and shape change across the embryo [2]. In cancer, increasing cell size is observed during the epithelial to mesenchymal transition [3]. To elucidate such collective motion in tissues, cell monolayers are often used as model multicellular systems. In confluent monolayers of epithelial cells, where cells interact through strong cell-cell junctions, the dependence of collective migration patterns on average cell density has been studied, although spatiotemporal fluctuations in density at short time scales and length scales have not been investigated [4–7]. The relationship between collective motion and density fluctuations has been explored in many active-matter systems like shaken granules, motor-driven protein filaments, and swimming bacteria [8–11]. In all of these systems, free space exists between the particles, providing freedom for large density fluctuations to occur. By contrast, there is no free space in confluent tissue cell monolayers so density fluctuations require corresponding changes in the projected area of cells. In time-lapse videos and snapshots of cells in the published literature, area fluctuations are readily observed [7,12,13], and we have recently demonstrated that these fluctuations in cell area correspond to cell volume fluctuations [14]. However, the link between cell volume fluctuations and collective motion has not been made, limiting our understanding of the role cell size and density play in collective motion in tissues. The characterization of density fluctuations and collective motion in cell monolayers is a crucial step that is necessary to guide further development of theoretical models of tissue.

Here we study fluctuations in the divergence of the velocity field in an epithelial monolayer. From phase contrast images we directly observe large, time-varying fluctuations in cell number density and cell size across the layer. To characterize these fluctuations, we compute the dynamic structure factor and the space-time autocorrelation function of the velocity divergence, finding patterns of collective squeezing and expansion in patches approximately 250 μm in diameter with a characteristic oscillation time of 3–4 h. We monitor the transport of fluid in and out of cells with a fluorescent dye that dilutes when cells expand and concentrates when cells contract. The same spectral and correlation analyses on fluorescence maps reveal that fluid travels between cells during these collective fluctuations. We also find that intercellular fluid flow is impeded by interfering with the fluid channels that connect cells. Taken together, these results uncover a potential physical coupling between cells involving pressure generation through contraction and intercellular fluid flow as a response.

II. RESULTS

To investigate collective cell motion, confluent islands of Madin Darby canine kidney (MDCK) epithelial cells are plated on glass-bottomed culture dishes coated with bovine collagen I. The cells are plated at a relatively low average density of 1400 cells per mm^2. To monitor fluid distribution in the layer, cells are treated with 20 μM 5-chloromethyl-fluorescein diacetate (CMFDA) in serum-free Dulbecco's modified Eagle's medium (DMEM) and 0.2% dimethyl sulfoxide (DMSO) for 40 min. DMSO permeabilizes the membrane, allowing dye to enter the cell body. After dye treatment, the dishes are washed and filled with DMEM supplemented with 10% fetal bovine serum and 1% penicillin streptomycin. In the absence of DMSO, CMFDA is a membrane-impermeable cytosol dye, so the movement of water in and out of a cell is detected by changes in the dye concentration; when a cell becomes larger, the fluorescence intensity per pixel drops, and when it becomes smaller, this intensity rises. These changes in cell size occur primarily in plane; our measurements show that cell height fluctuations are small compared to cell area fluctuations [14]. We image cells at 37 °C in 5% CO_2 on an inverted microscope in phase contrast and fluorescein isothiocyanate (FITC) fluorescence every minute. We monitor approximately 660 cells over six h and observe oscillating

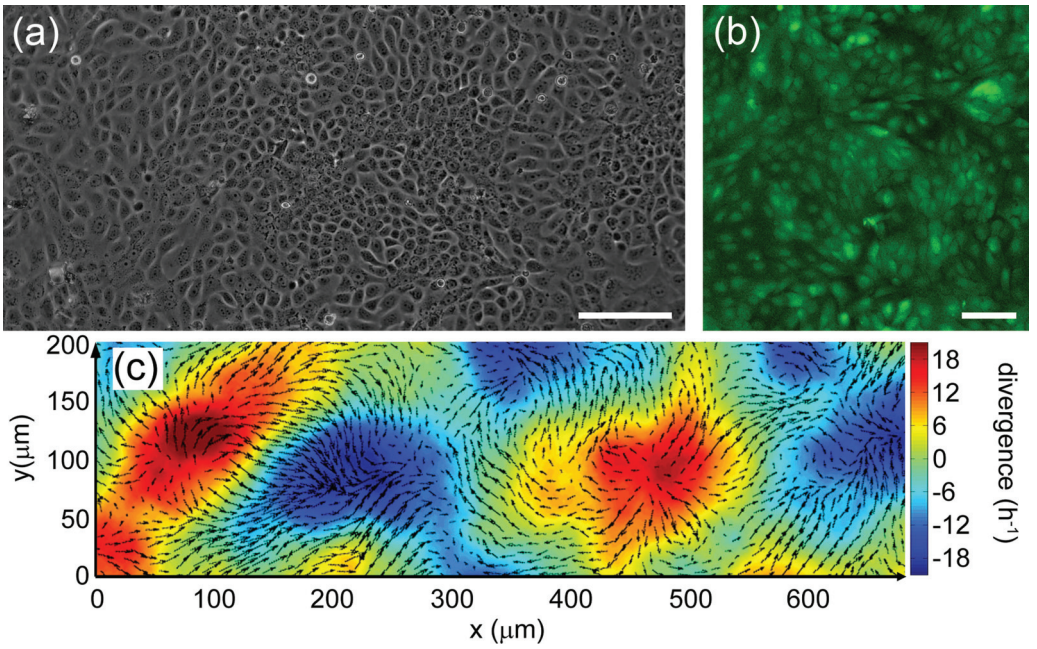

FIG. 1. (Color) (a) Phase contrast microscopy of a confluent MDCK monolayer exhibits a patchy, heterogeneous cell number density distribution; scale bar = 150 μm. (b) To study fluid flow between regions of cells, the layer is dyed with membrane-impermeable dye that concentrates and dilutes with changes in cell volume; scale bar = 100 μm. (c) Velocity fields of cell motion superimposed on top of divergence fields show coherent patterns of spreading (positive) and contracting (negative) regions spanning hundreds of microns.

patches of increasing and decreasing cell density spanning many cell diameters [see Figs. 1(a) and 1(b) and Movies S1 and S2 in the Supplemental Material [15]].

A. Velocity and divergence fields

We measure cell velocity fields using particle image velocimetry (PIV) in PIVLab software with two levels of recursive fast Fourier transforms to produce approximately 2.2×10^4 velocity vectors per frame [Fig. 1(c)] [16]. Simple metrics of cell motion can be determined from these velocity fields. For example, average local motion within the layer is captured by the root-mean-square (rms) speed at each point in space, $\sqrt{\langle \mathbf{v} \cdot \mathbf{v} \rangle_t}$, having an average value of 11.9 μm/h across the entire layer with a standard deviation of 4.4 μm/h. This migration speed agrees with the speed previously reported in MDCK monolayers at low cell density [6,17]. The layer exhibits slightly slower global migration speed of 9.9 μm/h with a standard deviation of 1.2 μm/h. This collective speed is determined from the magnitude of the mean velocity in space $|\langle \mathbf{v} \rangle_{\mathbf{r}}|$, vector averaged over the 1×1.3 mm^2 field of view and then averaged over time. More complicated metrics of motion within the cell layer like the divergence, described below, inherently remove this global motion.

We compute the divergence $\nabla \cdot \mathbf{v}$ throughout the layer, where positive values correspond to expanding cells and negative values correspond to contracting cells. A 30 min boxcar time average is performed on each velocity vector to smooth out short-time-scale fluctuations before computing the divergence. Additionally, rather than computing $\nabla \cdot \mathbf{v}$ from discrete differences between neighboring vectors, we employ the divergence theorem to calculate the average divergence over small regions. At each location in space, the scalar product is taken between a ring of velocity vectors and a normal-vector kernel and then integrated (see the Supplemental Material [15], Fig. S1). We validate this method with tests on model velocity fields, comparing them to analytically determined divergence fields, and find about 4% error. We also explore potential artifacts generated by the choice of kernel radius. With our experimental data, using a kernel radius less than 35 μm, the divergence begins to strongly reflect single-cell fluctuations. Using kernels of radii anywhere between 75 and 130 μm produces consistent space-time patterns, while using kernels much larger than 130 μm washes out the large-scale patterns, which have a correlation length of about 250 μm, described later. An example divergence map is shown in Fig. 1(c), where a 75 μm kernel was used. At any time, a patchy distribution of alternating diverging and converging regions is measured, similar to the sizes of cell clusters we observe by eye from phase contrast images. Time-lapse videos of these divergence maps show dramatic oscillations over the course of several hours [Fig. 1(c) and Movie S3 in the Supplemental Material [15]).

B. Spectral analysis of divergence and fluorescence

To characterize the dynamics of collective volume fluctuations and associated fluid transfer in cell layers we calculate the dynamic structure factor of both divergence fields and fluorescence intensity maps. The normalized dynamic structure factor $S(q,\omega)/S(q)$ is computed from the squared modulus of the Fourier transform of a variable in space and time, and the integral of $S(q,\omega)$ over frequency gives the static structure factor $S(q)$. The dynamic structure factor measures the relative Fourier components of a spatiotemporally fluctuating variable. Traditionally, $S(q,\omega)/S(q)$ is measured directly from inelastic x-ray, neutron, or light scattering to monitor density

fluctuations throughout space and time in a material. Here we measure $S(q,\omega)/S(q)$ by Fourier transforming divergence fields and fluorescence images. Transient effects associated with cell proliferation are found to be small in the system measured here. We monitor the average cell density, finding approximately an 8% increase throughout the course of the experiments, similar to previous observations [14].

Both the divergence and fluorescence spectra exhibit broad peaks in ω that shift with wave vector q. To measure the positions and widths of these features we fit two line shapes: a central Lorentzian peak and a damped harmonic oscillator (DHO) spectrum [18,19],

$$\frac{S(q,\omega)}{S(q)} = I_0(q)\frac{\frac{1}{2}\Gamma_0(q)}{\omega^2 + \left[\frac{1}{2}\Gamma_0(q)\right]^2} + I(q)\frac{\Omega(q)\Gamma^2(q)}{\left[\omega^2 - \Omega^2(q)\right]^2 + \omega^2\Gamma^2(q)}.$$

The central Lorentzian is a Rayleigh peak with amplitude $I_0(q)$ and width $\Gamma_0(q)$, which arises from stochastically relaxing density fluctuations. The second term describes Brillouin peaks located at $\pm\Omega(q)$ with amplitude $I(q)$ and widths $\Gamma(q)$ corresponding to density fluctuations with elasticlike responses to driving forces [Fig. 2(a)]. The collective motion investigated here is captured by the dispersion relations of the Brillouin peaks $\Omega(q)$ and the associated peak widths $\Gamma(q)$. Unrestricted forms of $\Omega(q)$ and $\Gamma(q)$ are determined by fitting the DHO spectrum to the data along the ω axis at every discrete wave vector, q, building up the dispersion relations point by point in reciprocal space. Nonlinear least-squares fitting is employed to determine the peak intensity, position, and width at each q location. The error bars shown in Figs. 2(b) and 2(c) for $\Omega(q)$ and $\Gamma(q)$ are the 95% confidence intervals of best-fit values.

The dispersion relation of divergence fluctuations shows two distinct regimes of motion: a low-q horizontal plateau and a high-q power law region. Throughout most of the measured dispersion relation, the half-width of the Brillouin peak, $\Gamma(q)/2$, is much less than $\Omega(q)$, which arises from oscillatory motion. The plateau at wavelengths larger than 250 μm shows that multicellular motion in the cell layer manifests as oscillating standing waves with zero group velocity and a characteristic period of 3 h. The average cell area in the monolayers is approximately 700 μm^2; treating the oscillating patches as circular with a radius of 125 μm, we find that about 70 cells expand and contract together in these standing wave patterns [Fig. 2(b)].

We were unable to obtain fits of $S(q,\omega)/S(q)$ from fluorescence intensity data at wavelengths larger than 80μm. Over the q range corresponding to 15–80 μm, the intensity dispersion relation shows no standing modes, but a dominant propagating mode that scales as q. We find $\Omega(q) > \Gamma(q)/2$ for this mode, which propagates with a group velocity of 25 μm/h. This speed is more than twice the speed of both single-cell migration and global collective migration, measured from PIV analysis. These features suggest that intercellular fluid waves rapidly traverse distances of three to four cell lengths before dispersing, which we explore further below. These mid-wavelength wavelike motions can be directly seen in false color maps of fluorescence intensity time-lapse movies [Fig. 2(c) and Movie S4 in [15]].

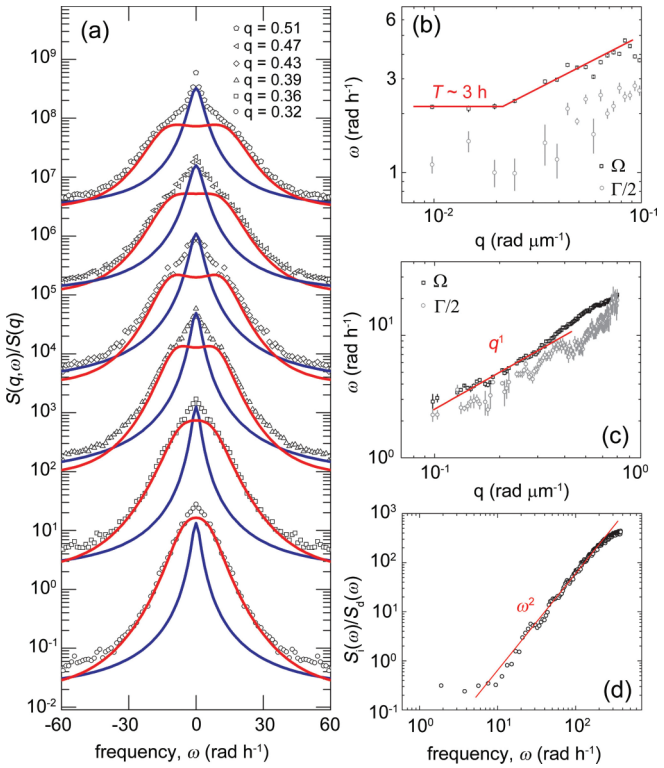

FIG. 2. (Color) (a) The dynamic structure factor $S(q,\omega)/S(q)$ is computed and fitted with Rayleigh (blue) and Brillouin (red) peaks to determine dispersion relations for divergent cell motion and intercellular fluid flow. (b) The divergence dispersion relation shows a standing wave mode at wavelengths longer than 250 μm with a characteristic period of ~3 h.) (c) The fluorescence intensity dispersion relation shows a propagating mode that scales like q with a group velocity of 25 μm/h. (d) The ratio of temporal Fourier transforms of intensity and divergence, $S_i(\omega)/S_d(\omega)$, scales as ω^2, showing that fluorescence intensity is proportional to the first time derivative of divergence.

To test the relationship between divergence fluctuations and fluid transport within the monolayer without the need for peak fitting, we compute the ratio of the two power spectra of fluctuations, $S_i(\omega)/S_d(\omega)$, where $S_A(\omega) = \langle|\mathcal{F}[A]|^2\rangle_{\mathbf{r}}$ is the space-averaged squared modulus of the Fourier transform in time. Here, the transformed variable A is either divergence, denoted by subscript d, or the fluorescence intensity, denoted by subscript i. We find that this ratio of spectra scales approximately as ω^2. Thus, at any location in space the fluorescence intensity is proportional to the first time derivative of the divergence. This relationship is expected to arise for coupled oscillating variables like dye concentration and divergence. An oscillating cell, when at its minimum size, has maximal fluorescence intensity and zero divergence, while a cell at its maximum size has minimal intensity and zero divergence; cells at their mean intensity are maximally diverging or converging [Fig. 2(d)].

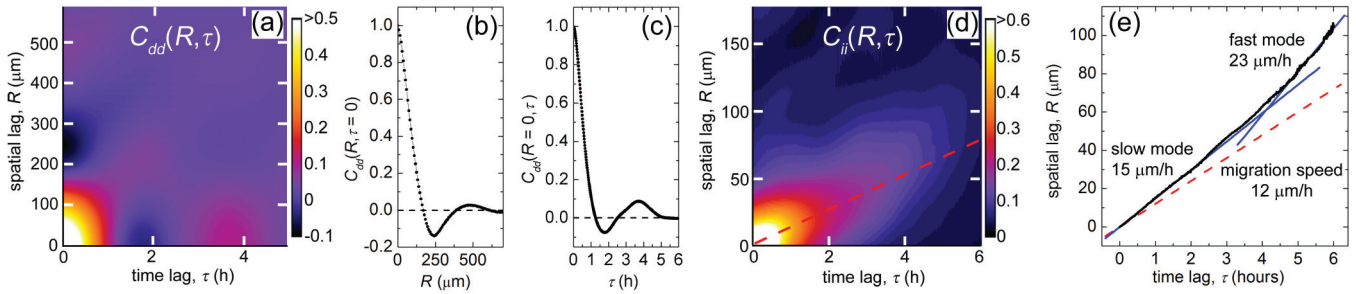

FIG. 3. (Color) The average space-time divergence autocorrelation function (a) reveals standing wave dynamics in the velocity field, exhibiting oscillations along R at $\tau = 0$ (b) and along τ at $R = 0$ (c). By contrast, the fluorescence intensity autocorrelation function (d) exhibits only a diagonal band of correlation and no significant oscillations, which arises from propagative motion. The slope of this feature is close to the single-cell migration speed (red dashed line) at short times but increases at long times and distances (e). We fitted lines to the contour of this correlation separately at short times and long times, finding speeds of $14.86 \pm 0.02\,\mu$m/h and $22.5 \pm 0.3\,\mu$m/h (blue lines are fits; $\pm$ ranges are 95% confidence intervals of fitted slopes).

C. Spatiotemporal correlation analysis

To check our interpretation of the dispersion relations from dynamic structure factor analysis, we compute real-space and real-time autocorrelation functions $C_{AA}(\mathbf{R},\tau) = \langle A(\mathbf{r},t)A(\mathbf{r}+\mathbf{R},t+\tau)\rangle_{\mathbf{r},t}$, where A is either divergence or intensity, and averages are performed over space $\mathbf{r}$ and time t. Correlations are normalized, resulting in $-1 \leqslant C_{AA} \leqslant 1$, where $C_{AA} = 1$ corresponds to 100% correlation. For $C_{dd}(\mathbf{R},\tau)$ we take an azimuthal average over all directions in space, finding strong, regular spatial and temporal patterns [Fig. 3(a)]. Instantaneous spatial correlations are captured by $C_{dd}(\mathbf{R},\mathbf{0})$, where we observe a strong anticorrelated spatial peak at $R = 250\,\mu$m, corresponding to the spacing between anticorrelated patches of converging and diverging cells [Fig. 3(b)]. Temporal fluctuations are captured by $C_{dd}(0,\tau)$, which shows a strong anticorrelation peak at approximately $\tau = 2$ h, corresponding to a period of about 4 h [Fig. 3(c)]. These signatures in the space-time correlation function of divergence in the monolayer paint the same picture as inferred from spectral analysis: space is tiled with diverging and converging multicellular patches that collectively oscillate out of phase with one another. The slight disagreement between the period measured from dispersion relations and the period measured from correlation functions most likely arises from determining the period in the latter case from peak positions; strong asymmetric broadening of correlation functions will shift the apparent peak positions relative to the true period.

The fluorescence intensity autocorrelation function $C_{ii}(\mathbf{R},\tau)$ exhibits irregular spatial patterns and is anisotropic. Thus, instead of taking an azimuthal average, we observe the C_{ii} along different azimuthal angles. Along most directions we see a linear diagonal band of intensity that starts at $R = 0$ and $\tau = 0$ and persists up to length scales of about 50 μm and time scales of about 2.5 h [Fig. 3(d)]. Such a diagonal band corresponds to propagative motion, with the slope giving the propagation speed. This band of intensity at short time and length scales overlays well, visually, with a line corresponding to the local migration speed of single cells. To determine the slope without fitting the complicated peak shape, we compute the first moment of intensity along the R direction at every lag time τ and accumulate a contour in R and τ. From a linear fit of this contour at short times, we find that the propagation speed is 15 μm/h, which is close to the 12 μm/h migration speed of individual cells. We therefore believe that C_{ii} is dominated by the translocation of individual cells at short time and spatial scales.

Using the same approach at longer time scales, we find that the slope of the band changes and generally increases, corresponding to a faster speed. This second mode is observed along all directions and has a slope between 14 and 43 μm/h depending on direction. The average speed of this second mode is 23 μm/h, which is much larger than both the single-cell migration speed and the global collective migration speed. However, this speed is close to the 25 μm/h group velocity found from dynamic structure analysis, above, and further suggests that fluid is rapidly transported over distances comparable to the spacing between diverging patches of cells, at correspondingly long time scales [Fig. 3(e)].

D. Inhibiting gap junction transport

To explore the role of intercellular fluid transport in cell volume fluctuations, we treat cells with a 100 μM solution of carbenoxolone (CBX). CBX is a water-soluble form of glycyrrhetinic acid shown to inhibit gap junction intercellular communication [1–3,20,21]. Cells are treated with CBX for 3 h, then dyed with 20 μM CMFDA in serum-free and antibiotic-free DMEM and 0.2% DMSO for 40 min. After dyeing, cells are resubmerged in full growth medium supplemented with 100 μM CBX and allowed to incubate for 1 h before time-lapse imaging.

Velocity fields of cell motion are measured and divergence is computed in the same way as described above for untreated cells. We find very little change in the rms migration speed within the layer ($6.1 \pm 2.9\,\mu$m/h) or global velocity ($4.2 \pm 1.4\,\mu$m/h). We compute the space and time autocorrelation functions for divergence fields and fluorescence intensity images, $C_{dd}(R,\tau)$ and $C_{ii}(R,\tau)$, respectively, as described in the previous section. $C_{dd}(R,\tau)$ exhibits the characteristics of a standing wave pattern, qualitatively resembling the divergence patterns in untreated cells. We find an anticorrelation peak in the divergence autocorrelation function $C_{dd}(R,0)$ located at a spatial shift of $R = 110\,\mu m$. Thus, cells treated with CBX have much smaller regions of coordinated convergence and divergence than undrugged cells. The local fluctuations in time

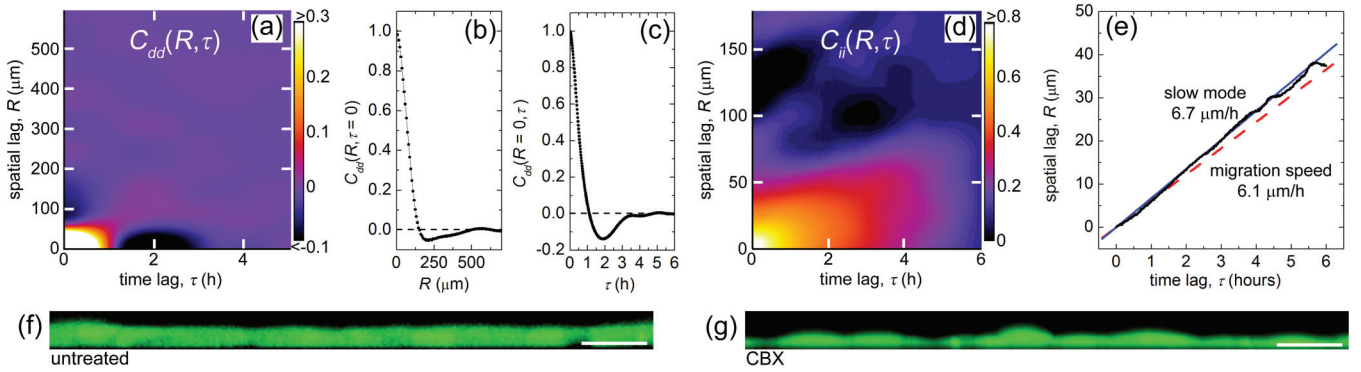

FIG. 4. (Color) The divergence autocorrelation function of cells treated with 100 μM CBX (a) shows distinct anticorrelation peaks at $R = 100\,\mu$m and $\tau = 2$ h (b),(c). (d) The fluorescence intensity autocorrelation function of CBX-treated cells exhibits a diagonal band of intensity that is much broader along the R direction than observed for undrugged cells. (e) A contour constructed from intensity-moment analysis has a slope of $6.7 \pm 0.01\,\mu$m/h, which suggests that the correlation function may reflect single-cell motion and potentially a dramatically reduced propagation of fluid between cells. (f) Confocal X-Z slices of an undrugged monolayer show a flat surface; scale bar $= 10\,\mu$m, while (g) X-Z slices of cells treated with CBX show a rough surfaces; scale bar $= 10\,\mu$m.

given by $C_{dd}(0,\tau)$ show that cells treated with CBX still exhibit an average oscillation period of 4 h, with an anticorrelation time lag of $\tau = 2$ h along τ. These results show that collective cell motion in CBX-treated cells qualitatively resembles the motion of undrugged cells, moving in a standing wave pattern composed of diverging and converging cell groups. However, since the characteristic wavelength of this standing wave is less than one-half that of the undrugged cells, the oscillating patches of CBX treated cells contain less than one-quarter of the number of cells moving together in undrugged layers [Figs. 4(a) and 4(c)]. Thus, inhibiting fluid flow through gap junctions dramatically reduces the domain size of collective density fluctuations within the layer.

It is possible that CBX-treated cells fluctuate out of plane in order to accommodate density fluctuations while having inhibited fluid transfer between cells. To test for potential cell thickness fluctuations, cell layers are imaged in confocal microscopy. X-Z slices of untreated MDCK cells are very flat [Fig. 4(f)]. By contrast, CBX-treated cells have a height profile that is significantly rougher: cells are thick near their centers but thin at their edges and all cells are not the same height. Analysis of the height fluctuations in CBX-treated monolayers, as described in Ref. [14], reveals a 40% standard deviation in layer thickness, which is much larger than the 5% fluctuations found in untreated monolayers. Thus, density fluctuations in monolayers with reduced intercellular fluid permeability may occur because of out-of-plane cell thickness variations.

The effects of inhibiting gap junctions are also seen in the fluorescence intensity dynamics. The fluorescence intensity autocorrelation function $C_{ii}(R,\tau)$ for cells treated with CBX exhibits a diagonal band of intensity in the R-τ plane that indicates propagative motion. In contrast to the case of undrugged cells, this band of intensity is very broad along R and does not appear to change slope along its contour. We estimate a propagation speed with the intensity moments analysis described in the previous section. The speed varies with direction, always having a value between 5 and 8 μm/h with an average value of 6.5 μm/h, which is comparable to the single-cell migration speed of 6.1 μm/h in CBX-treated layers. A line with slope 6.1 μm/h almost overlays a contour of data extracted from C_{ii} (measured along a direction representative of the average behavior). Thus, if fluid transport occurs in CBX-treated cells, it moves at less than or equal to the cell translocation speed, which is much slower than the fluid transfer speed between undrugged cells [Figs. 4(d) and 4(e)]. These results and the absence of faster secondary bands of intensity along any direction of $C_{ii}(R,\tau)$ further suggest that the fast-propagating modes observed in undrugged monolayers correspond to intercellular fluid flow.

E. Estimating pressure fluctuations in the monolayer

For cells to collectively contract and expand while exchanging fluid, they must actively generate pressure to overcome viscous drag forces associated with fluid flow through gap junction channels. Within each volume element in the monolayer, we estimate the local deviation in pressure relative to the average pressure in the rest of the layer by employing Darcy's law $\Delta P(x,y) = Q(x,y)/k$, where $Q(x,y)$ is the local volume flow rate into or out of the location and k is the permeability of a cell, which we previously estimated to be $0.06\,\mu\text{m}^3\,\text{kPa}^{-1}\,\text{s}^{-1}$ [14]. We compute $Q(x,y)$ from the divergence $\nabla \cdot \mathbf{v}(x,y) = -Q(x,y)/V$, where V is the volume of a voxel with the height of an average MDCK cell, $h_c = 7\,\mu$m. Thus, if a patch of cells is increasing in density, $\nabla \cdot \mathbf{v}(x,y)$ is negative and $Q(x,y)$ and $\Delta P(x,y)$ are positive, denoting that fluid is leaving the region driven by a high pressure. Conversely, if cells in a region are becoming less dense, $Q(x,y)$ and $\Delta P(x,y)$ are negative, reflecting that fluid is entering the region. The resulting pressure distribution has the same spatial patterns as the divergence fields, above, and at any point in time the difference between minimum and maximum pressure estimates spans about 200 Pa (Fig. 5).

F. Driving cell-cell fluid transport with monolayer indentation

To test whether these modest pressure gradients may drive fluid between cells within the layer, we manually apply pressure to a small region on the monolayer surface, observing fluid flow away from the pressure source (Fig 6). MDCK cell layers plated on glass substrates are dyed with 2.5 μM calcein

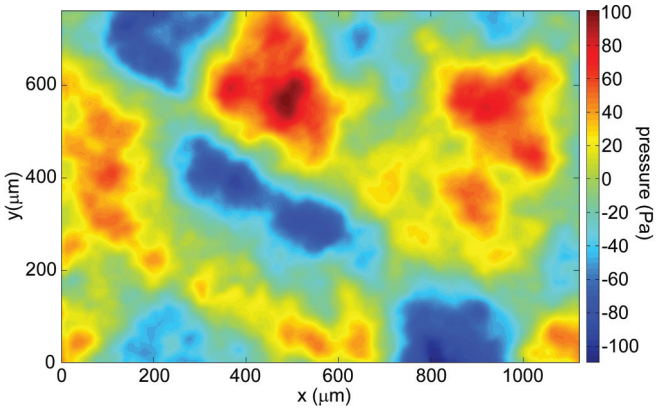

FIG. 5. (Color) A pixel-by-pixel pressure difference map estimated from velocity divergence. Positive values are associated with regions of contracting cells expelling fluid. Negative values are associated with regions of expanding cells. At any time these pressure fluctuations occur between +100 and −100 Pa about zero.

acetoxymethyl ester, a gap-junction-permeable cytosol dye, in serum-free DMEM and 0.25% DMSO. Since calcein can freely move through gap junction channels, we monitor fluid flow between cells by measuring changes in integrated calcein intensity. A polished borosilicate glass hemisphere of radius 3.1 mm, with surface roughness measured to be <10 nm by scanning white light interferometry, is used as the indenter.

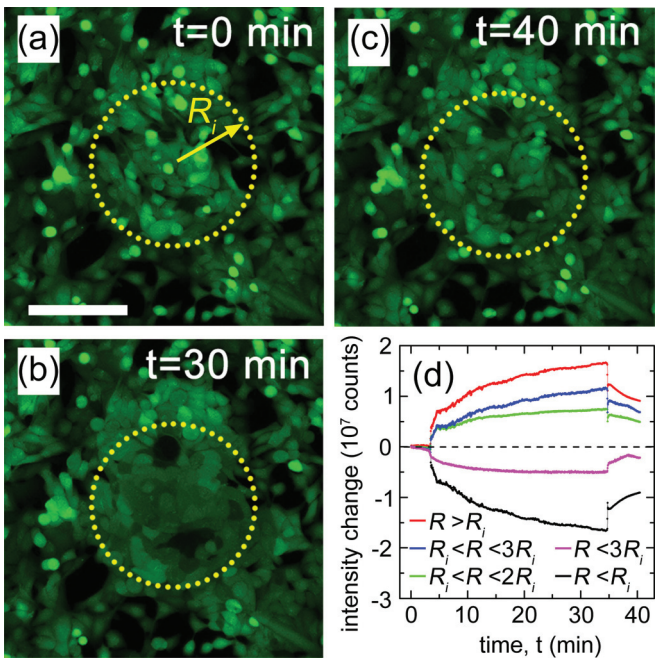

FIG. 6. (Color) MDCK monolayer dyed with calcein fluorescent dye (a) before (scale bar = 150 μm), (b) during, and (c) after indentation. The radius of the contact area, R_i, is denoted by the yellow dotted line. By comparing (a) and (c) it can be seen that cell shape recovers with little or no damage to the monolayer. (d) Change in integrated dye intensity inside the contact area ($R < R_i$) and outside the contract area ($R > R_i$) during indentation show transport of fluid and regions of varying size show systematic changes in transported dye with distance from the pressure source.

The hemisphere is cleaned using water and ethanol between experiments, and is conditioned in the media bath for at least 5 min prior to contacting the cell monolayer.

On an open-platform microindentation system [4], a 250 μm stroke piezoelectric stage with reported resolution of 0.7 nm moves the probe normal to the cell layer to apply the normal force. The nascent cell surface is not touched before the experiment is started. Over a loading time of ∼10 s, the force rises from 0 to 50 μN and remains there for 35 min using force feedback at 12.8 Hz. The displacement per step is limited to 8 nm to avoid damaging the cell layer due to noise. We measure force by reading the displacement of a flexure (stiffness 144.5 μN/μm) through which the force is applied. Capacitive sensors of reported rms resolution 14 nm have sensitivity of 0.2 V/μm over a range of 100 μm at a standoff of 100 μm from the flexure target. In this configuration, force detection has a resolution of 2 μN. Steady-state applied forces were measured to be 50 ± 7 μN over the 35-min experiment, corresponding to pressures of about 1 kPa.

Over the course of indentation we directly observe cells compressing under the contact. After the probe is removed, these cells immediately recover their size, shape, and location, with no visible damage imparted to the layer during indentation [Figs. 6(a)–6(c)]. Measurements of the integrated intensity of cells underneath the contact, for radii R less than the contact radius R_i, show a dramatic decrease in intensity throughout the contact duration and then a small recovery after the pressure is released [Fig. 6(d)]. The sharp rise in the integrated intensity of cells outside the contact area, $R > R_i$, shows that fluid containing calcein is driven out of cells under the contact into neighboring cells. A small accumulation of dye occurs immediately outside the contact ($R_i < R < 2R_i$), and more total fluorescence intensity is accumulated in larger regions outside the contact. Within the region $R < 3R_i$, nearly all of the fluorescence intensity is recovered after removal of the pressure source.

III. CONCLUSION

These results demonstrate that groups of cells in a monolayer exhibit collective divergent velocity fluctuations that occur in concert with cell volume change, consistent with single-cell volume fluctuations observed previously [14]. Unlike other systems of active particles, there is no free space between cells in a confluent layer. Thus, collective density changes and cell volume fluctuations must involve the flow of intracellular fluid, most likely water. Water can be transported across the cell membrane in exchange with the cell growth medium bath, or transported between cells through groups of fluid channels known as gap junctions. The measurements described here enable us to distinguish between these two means of water transport, and we find repeatedly that fluid moves between cells in conjunction with cell volume changes.

If cellular water is primarily exchanged with the bath to accommodate in-plane divergences, the intensity dispersion relation and correlation function should show standing modes with similar periods and length scales as the divergence dispersion and correlation function. This is because the group velocity of water within the layer must be zero in such a case, apart from the potential contribution from cell

migration. However, no standing modes are observed in either the intensity correlation function or the intensity dispersion relation. By contrast, fast-propagating modes are present in both the fluorescence intensity correlation and dispersion relations. This type of signal would arise from driven fluid transport between cells in the monolayer. In this case, local fluctuations in water content or dye concentration would have a large group velocity, as we observe. These two types of transport can be thought of in analogy to the process of moving a pile of stones from one location to another. A standing-wave-like dynamic would occur when removing a stone from one pile and placing it in another pile. A propagating-wave-like dynamic would occur if stones were pushed from one pile to another. In both cases, the same task can be achieved, but the space-time correlations differ. It should be noted that this contrast between ideal, extreme cases is bound to be modified by complications like heterogeneous dye loading from cell to cell, and by cell migration, which generates fluorescence intensity changes in space and time without necessarily involving water transport. Furthermore, we do not propose that water exchange does not occur with the surrounding bath, but rather that cellular water is significantly displaced from cell to cell during collective motion in the monolayer. In-depth studies that employ techniques like fluorescence recovery after photobleaching may help to further elucidate the detailed balance between multiple avenues for water transport.

The pressure differences estimated here hint that cell-to-cell osmotic pressure gradients may be sufficient to drive intercellular fluid flow. Quick volume recovery observed in single-cell measurements of water transport due to osmotic pressure suggests that ion transport can generate osmotic pressures on the order of 100 Pa [22]. Thus, a group of cells could adjust local cell volume by modulating ionic uptake. Contracting cells could be responding to osmotic pressure gradients generated by neighboring spreading cells that have increased ion transport. Alternatively, forces imparted by cytoskeletal contractions on internal cytosolic fluid could be another source of fluid driving pressure. Regularly, traction force measurements of migrating monolayers report contractile stresses in the range of hundreds of pascals, comparable to the pressures we estimate here required for intercellular fluid flow [12,13]. Ultimately, the source of intercellular fluid pressures is probably a combined effect of both osmotic and cytoskeletal stresses and deserves greater study.

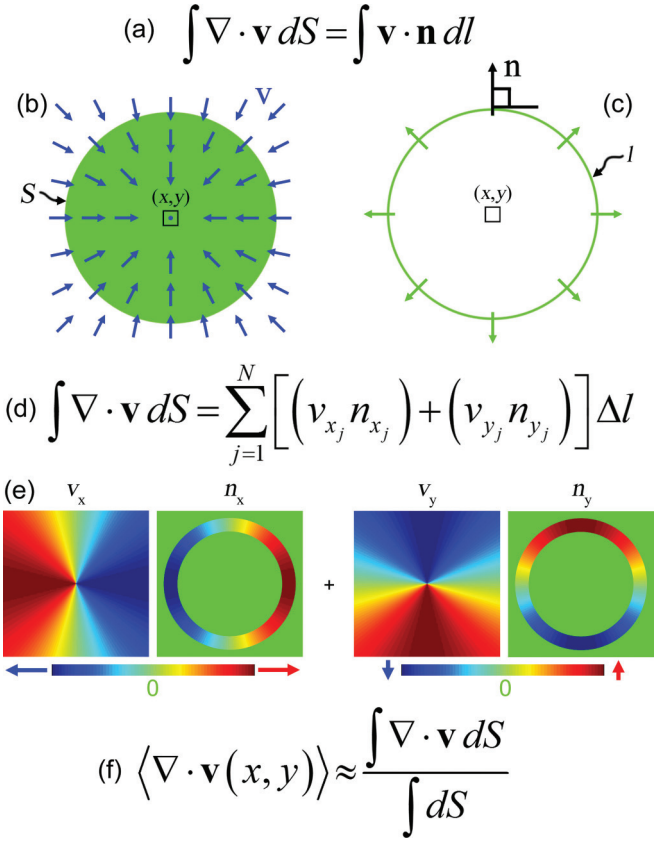

FIG. 7. (Color) (a) The divergence theorem relates the total divergence of a velocity vector field **v** within area S to the line integral of the components of the velocity vectors normal to the area boundary l. (b) Schematic of a converging vector field with area S centered about point (x,y). (c) Schematic of boundary line l defined by normal vectors **n**. (d) The divergence of the velocity field is computed by taking the sum of the product of v_x and n_x and the product of v_y and n_y for all N discrete positions, Δl, around the boundary line. (e) Visual representation of equation in (d) for the converging velocity field. Red represents positive vectors and blue represents negative vectors in a right-handed coordinate system and green represents a value of zero. (f) The average divergence at a point (x,y) is approximated as the divergence divided by the area in S. This process is performed at each vector position to determine the divergence map of the whole cell motion velocity field.

ACKNOWLEDGMENT

This project was funded by NSF Grant No. CMMI-1161967.

APPENDIX

We compute the local average divergence in the cell velocity fields, **v**, using the divergence theorem. In two dimensions, the divergence theorem states that the total divergence of all vectors within an area S is equivalent to the line integral of the components of the velocity vectors normal to the boundary of the area, l. For example, if more vectors are entering the boundary than leaving, the vectors within the area are converging. We begin calculating the divergence by defining a ring shaped kernel **n** that represents the unit vectors normal to l. We express the line integral along l as the sum of the product of the x components of the velocity field v_x and line normal vectors n_x with the product of their corresponding y components v_y and n_y at all N positions around the kernel. In this way we compute the divergence at every location (x,y) in **v**. To determine the average divergence we normalize by the total area of S (Fig. 7).

[1] P. Friedl and K. Wolf, J. Cell Biol. **188**, 11 (2010).

[2] C. Tickle, *Principles of Development* (Oxford University Press, Oxford, UK, 2011).

[3] S. Lamouille and R. Derynck, J. Cell Biol. **178**, 437 (2007).
[4] M. Poujade, E. Grasland-Mongrain, A. Hertzog, J. Jouanneau, P. Chavrier, B. Ladoux, A. Buguin, and P. Silberzan, Proc. Natl. Acad. Sci. USA **104**, 15988 (2007).
[5] L. Petitjean, M. Reffay, E. Grasland-Mongrain, M. Poujade, B. Ladoux, A. Buguin, and P. Silberzan, Biophys. J. **98**, 1790 (2010).
[6] T. E. Angelini, E. Hannezo, X. Trepat, M. Marquez, J. J. Fredberg, and D. A. Weitz, Proc. Natl. Acad. Sci. USA **108**, 4714 (2011).
[7] A. Puliafito, L. Hufnagel, P. Neveu, S. Streichan, A. Sigal, D. K. Fygenson, and B. I. Shraiman, Proc. Natl. Acad. Sci. USA **109**, 739 (2012).
[8] M. C. Marchetti, J. F. Joanny, S. Ramaswamy, T. B. Liverpool, J. Prost, M. Rao, and R. A. Simha, Rev. Mod. Phys. **85**, 1143 (2013).
[9] V. Narayan, S. Ramaswamy, and N. Menon, Science **317**, 105 (2007).
[10] V. Schaller and A. R. Bausch, Proc. Natl. Acad. Sci. USA **110**, 4488 (2013).
[11] H.-P. Zhang, A. Be'er, E.-L. Florin, and H. L. Swinney, Proc. Natl. Acad. Sci. USA **107**, 13626 (2010).
[12] X. Trepat, M. R. Wasserman, T. E. Angelini, E. Millet, D. A. Weitz, J. P. Butler, and J. J. Fredberg, Nat. Phys. **5**, 426 (2009).
[13] D. T. Tambe *et al.*, Nat. Mater. **10**, 469 (2011).
[14] S. M. Zehnder, M. Suaris, M. C. Bellaire, and T. E. Angelini, Biophys. J. **108**, 247 (2015).
[15] See Supplemental Material at http://link.aps.org/supplemental/10.1103/PhysRevE.92.032729 for videos of cell motion, divergence fluctuations, and fluorescence intensity fluctuations.
[16] W. Thielicke and E. J. Stamhuis, J. Open Res. Software **2**, e30 (2014).
[17] T. E. Angelini, E. Hannezo, X. Trepat, J. J. Fredberg, and D. A. Weitz, Phys. Rev. Lett. **104**, 168104 (2010).
[18] G. Ruocco and F. Sette, J. Phys.: Condens. Matter **11**, R259 (1999).
[19] H. Dekker, Phys. Rep. **80**, 1 (1981).
[20] J. S. Davidson and I. M. Baumgarten, J Pharmacol. Exp. Therapeut. **246**, 1104 (1988).
[21] R. J. Thompson, N. Zhou, and B. A. MacVicar, Science **312**, 924 (2006).
[22] S. K. Pierce and A. D. Politis, Annu. Rev. Physiol. **52**, 27 (1990).